

## Article

# Research on High-Torque-Density Design for Axial Modular Flux-Reversal Permanent Magnet Machine

Shan Lin <sup>1</sup>, Lanchao Chang <sup>2</sup>, Peng Su <sup>3,\*</sup>, Yongjian Li <sup>3</sup>, Wei Hua <sup>4</sup> and Yi Shen <sup>3</sup><sup>1</sup> Guangzhou Metro Design and Research Institute Co., Ltd., Guangzhou 510010, China<sup>2</sup> Laboratory of Electromagnetic Field and Electrical Apparatus Reliability, Hebei University of Technology, Tianjin 300401, China<sup>3</sup> State Key Laboratory of Reliability and Intelligence of Electrical Equipment, Hebei University of Technology, Tianjin 300130, China<sup>4</sup> School of Electrical Engineering, Southeast University, Nanjing 210096, China

\* Correspondence: supeng@hebut.edu.cn

**Abstract:** The traditional flux reversal permanent magnet (FRPM) machine has high torque ripple due to the double salient-pole structure, and the effective air-gap length is increased by the permanent magnet structure of the stator tooth surface, which affects the size of the air-gap magnetomotive force (MMF). This paper proposes an axial modular flux-reversal permanent magnet (AM-FRPM) machine with attractive torque capabilities. Based on air-gap magnetic field modulation theory, a method to achieve optimal air-gap harmonic torque contributions was developed. Then, the principle for high-torque-density generation in the AM-FRPM machine under an alternating magnetization topology was investigated using the PM magnetic field modulation and armature reaction magnetic field modulation. In addition, the cogging torque suppression mechanism, which guides the selection of stator-slot and rotor-pole combinations, was investigated. In addition, a comprehensive comparison of the electromagnetic characteristics of two AM-FRPM machines and a traditional FRPM machine was conducted. Then, the advantages and disadvantages of the three machines were analyzed. Finally, prototypes were manufactured and tested to verify the correctness of the theoretical analysis.

**Keywords:** flux-reversal permanent magnet machine; axial modular; PM magnetization modes; air-gap magnetic field modulation



**Citation:** Lin, S.; Chang, L.; Su, P.; Li, Y.; Hua, W.; Shen, Y. Research on High-Torque-Density Design for Axial Modular Flux-Reversal Permanent Magnet Machine. *Energies* **2023**, *16*, 1691. <https://doi.org/10.3390/en16041691>

Academic Editor: Anibal De Almeida

Received: 19 December 2022

Revised: 17 January 2023

Accepted: 31 January 2023

Published: 8 February 2023



**Copyright:** © 2023 by the authors. Licensee MDPI, Basel, Switzerland. This article is an open access article distributed under the terms and conditions of the Creative Commons Attribution (CC BY) license (<https://creativecommons.org/licenses/by/4.0/>).

## 1. Introduction

For electric vehicle and hybrid electric vehicle applications, high torque density and low torque ripple in PM machines are key performance metrics [1,2]. The FRPM machine has the advantages of a wide speed range, robust rotor structure, and reliable operation, making it suitable for driving systems [3].

The PM mounted on the stator-tooth surface increases the equivalent air-gap length of the FRPM machine, which affects the amplitude of the air-gap magnetomotive force, restricting the torque capability [4,5]. Based on the topology of the FRPM machine, a structure with internal and external double stators has been proposed [6]. The output torque was increased by installing PMs on the outer stator and rotor, but the overload capacity was reduced due to magnetic saturation. Similarly, the authors of [7] embedded the PMs in the stator slots of an FRPM machine, which helped improve the torque density. However, high magnetic loads caused significant core losses and reduced the efficiency [7]. An asymmetric stator-pole FRPM machine was proposed in [8] that could reduce the interpolar flux leakage and improve the torque capability. In addition, an FRPM machine with toroidal windings, resulting in higher torque and better efficiency than its counterpart with concentrated windings due to the high winding factors, has been proposed [4].

FRPM machines exhibit high cogging torque and torque ripple because of the salient-pole rotor structure [9]. The use of a groove structure for the stator teeth can effectively

suppress the cogging torque. However, this method increases the saturation of the stator teeth and limits the overload capability [10]. A structure with pairwise distribution of large and small teeth has been proposed. As the difference in space between the large and small teeth is  $180^\circ$ , the cogging torques generated by the large and small teeth have the opposite phase. Thus, the cogging torque can be reduced by matching different tooth widths. However, this method only applies to pole rotors [11]. The cogging torque can also be reduced by using unconventional structures, such as rotor asymmetry [12], asymmetric magnets [13], double stators [14], and tooth shaping [15,16]. However, these methods lead to the introduction of harmonics and reduce efficiency. For PM machines with a salient-pole rotor structure, the operation principle can be explained using the theory of magnetic field modulation [17,18]. The principle and the conditions necessary for generating a back electromotive force in the FSPM machine can thereby be obtained and the requirements for the generation of stable electromagnetic torque determined [19,20]. Therefore, it is worth investigating the reduction of cogging torque from the perspective of magnetic field modulation theory, but there are few studies in this area [21].

To further improve the torque density of FRPM machines and suppress torque ripple, this paper proposes an axial modular flux-reversal permanent magnet (AM-FRPM) machine based on the flux modulation principle. In Section 2, two different magnetization modes for AM-FRPM machines are introduced: axial modular alternant (AMA) magnetization and axial modular consequent (AMC) magnetization. In Section 3, the principle for achieving high torque performance in AMA-FRPM machines is investigated based on air-gap magnetic field modulation theory. In addition, the cogging torque suppression mechanism, which guides the selection of stator-slot and rotor-pole combinations, is analyzed. In Section 4, to investigate the advantages and disadvantages of AM-FRPM machines, a comprehensive comparison of the electromagnetic characteristics of two AM-FRPM machines and conventional FRPM machines is described. Finally, prototypes were manufactured and tested to verify the correctness of the theoretical analysis.

## 2. AM-FRPM Machine Topology

The topology of the AM-FRPM machine comprises two modular units with the same front and rear structures, as shown in Figure 1. The stator consists of two axially distributed stator module elements with the same structure, and a magnetic separation ring is embedded between the two modular units at the front and back of the stator to reduce the axial magnetic leakage of the AM-FRPM machine. The topology of the AM-FRPM machine module unit is similar to the conventional FRPM machine structure, as shown in Figure 2. The toroidal armature winding is wound in the stator yoke, which is composed of two modular units to improve the machine winding factor and the machine torque density. The two PMs of the stator teeth of the two modular units at the same position have opposite magnetization directions. An air gap is created between the two permanent magnets under the surface of the tooth of the same stator module to suppress torque ripple. The difference between the spatial positions of the rotor teeth of the front and rear rotor modules is  $\pi/P_r$  (where  $P_r$  is the number of rotor teeth;  $P_r = 8$  in this paper), which is used to eliminate even harmonics in the permanent magnet flux, improve the sinusoidal characteristics of the no-load permanent magnet flux waveform, and reduce torque ripple.

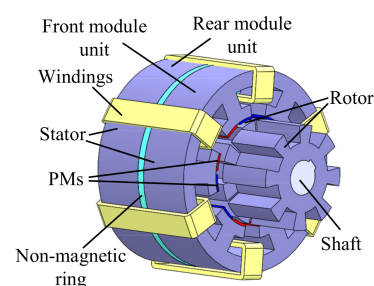


**Figure 1.** Topology of AM-FRPM machine.

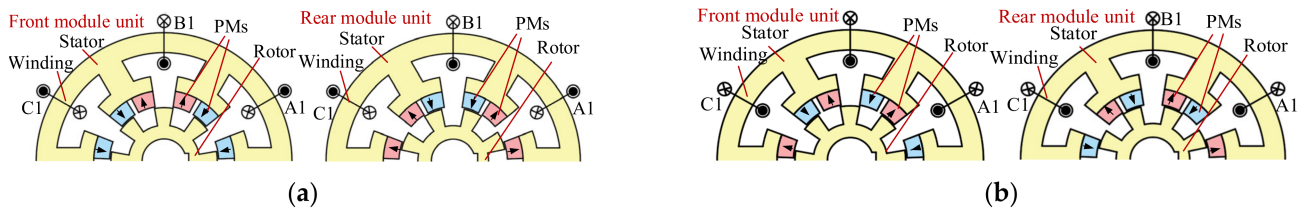


**Figure 2.** Axial modular structures of AM-FRPM machines. (a) AMA-FRPM topology. (b) AMC-FRPM topology.

In accordance with their different magnetization modes, AM-FRPM machines are divided into AMA-FRPM machines and AMC-FRPM machines, as shown in Figure 2. In the AMA-FRPM machine, the PMs under the same stator teeth in each stator module are magnetized in opposite directions, and the PMs located on both sides of the stator slots are magnetized in the same direction. In each stator module of the AMC-FRPM machine, the magnetization directions of the PMs on the same stator teeth are opposed, and those of the PMs on both sides of the stator slots are also opposed. The PM magnetization modes mentioned above are radial magnetization modes.

### 3. Operation Principle for AM-FRPM Machines

In AM-FRPM machines using the AMA and AMC magnetization methods, the salient rotor modulates the PM magnetic field and armature reaction magnetic field. The machines then have different harmonic distributions. This section investigates the operation principle for AM-FRPM machines with the two magnetization methods based on air-gap magnetic field modulation theory.

#### 3.1. PM Field Modulation

The harmonic distributions of the PM field in AM-FRPM machines can be analyzed with the magnetomotive force (MMF) permeance model, where the PM-MMF is assumed to be a rectangular wave, as shown in Figure 3, and the permeability of the iron core is infinite. The PM-MMF  $F_{PM}$  values for the front and rear modules are identical.

$$F_{PM}(\theta) = \pm \sum_{n=1}^{\infty} F_{PM-AMA_n} \sin(nP_s\theta/2), \tag{1}$$

where  $P_s$  is the number of stator slots, and  $F_{PM-AMA_n}$  is the PM-MMF coefficient.

$$F_{PM-AMA_n} = \frac{8F_{PM-AMA}}{n\pi} \sin \frac{n\pi}{2} \sin \frac{nP_s\theta_{PM-AMA}}{4} \cos \left\{ \frac{nP_s}{4} \left( \frac{\pi}{3} - \beta_{s-AMA} - \theta_{PM-AMA} \right) \right\}, \tag{2}$$

where  $\beta_{s-AMA}$  is the half-slot width between the PMs of the AMA-FRPM machine, and  $\theta_{s-AMA}$  and  $\theta_{PM-AMA}$  are the stator-slot and PM widths, respectively.  $F_{PM-AMA}$  is the PM-MMF amplitude.

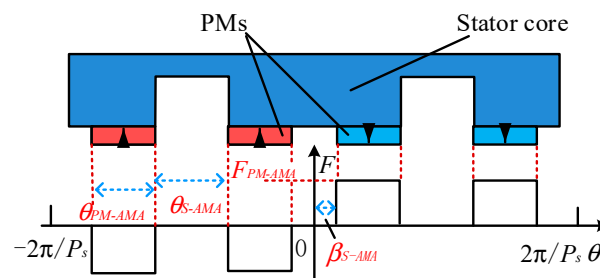


**Figure 3.** PM-MMF model of AMA-FRPM machine.

Equation (1) shows that the PM-MMF mainly includes harmonics with orders of  $nP_s/2$  ( $n = 1, 3, 5 \dots$ ). It is worth noting that the harmonic amplitude of the PM-MMF increases first and then decreases with the increase in the order of the harmonics, and Equation (2) indicates that the magnitudes of the third and ninth harmonics are the highest. Figure 4 shows the PM-MMF harmonic distribution obtained using finite element analysis (FEA), which verifies the results of the previous analysis.

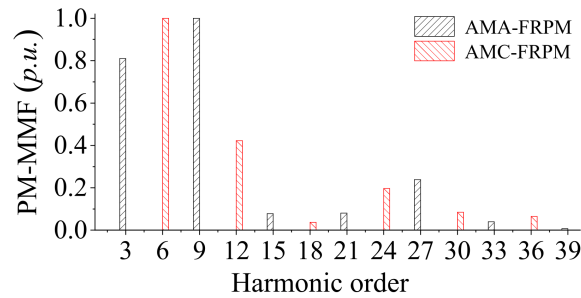


Figure 4. PM-MMF harmonic distribution for AM-FRPM machines.

The rotor permeance model for the front and rear module units is shown in Figure 5, where  $\theta_{rt-AMA}$  is the rotor tooth width, and  $\lambda_{rt}$  and  $\lambda_{rs}$  are the air-gap permeances of the rotor teeth and rotor slots, respectively. The front modular unit rotor permeance  $\lambda_{f-AMA}$  and rear modular unit rotor permeance  $\lambda_{r-AMA}$  are expressed as:

$$\lambda_{f-AMA}(\theta, t) = \lambda_{0-AMA} + \sum_{k=1}^{\infty} \lambda_{k-AMA} \cos kP_r(\theta + \omega_r t + \theta_0), \tag{3}$$

$$\lambda_{r-AMA}(\theta, t) = \lambda_{0-AMA} + \sum_{k=1}^{\infty} \lambda_{k-AMA} \cos kP_r(\theta + \omega_r t + \theta_0 + \frac{\pi}{8}), \tag{4}$$

where  $\lambda_{0-AMA}$  and  $\lambda_{k-AMA}$  are the Fourier coefficients of the rotor air-gap permeance,  $\omega_r$  is the rotor angular velocity, and  $\theta_0$  is the initial position of the rotor. Therefore, the no-load PM air-gap flux density of the front and rear module units of the AMA-FRPM machine can be obtained.

$$B_{AMA}(\theta, t) = \pm \sum_{n=1}^{\infty} \lambda_{0-AMA} F_{PM-AMA n} \sin(nP_s\theta/2) \pm \sum_{n=1}^{\infty} \sum_{k=1}^{\infty} \frac{\lambda_{k-AMA} F_{PM-AMA n}}{2} \sin[(nP_s/2 \pm kP_r)\theta \pm kP_r(\omega_r t + \theta_0)] \tag{5}$$

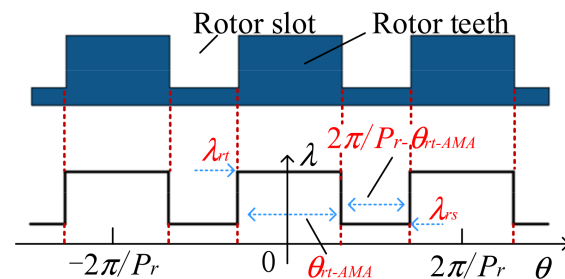
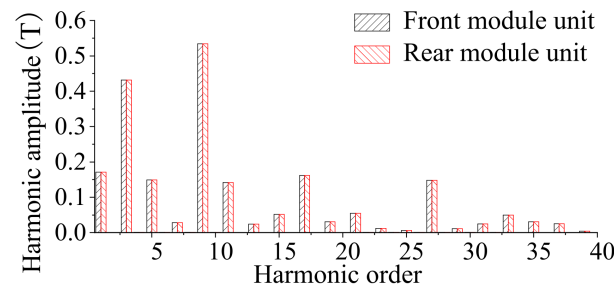


Figure 5. Permeance model for AMA-FRPM machine rotor teeth.

The harmonic distribution of the air-gap flux density can be obtained from Equation (5). The main harmonic orders are  $|nP_s/2 \pm kP_r|$  ( $n = 1, 3, 5 \dots, k = 0, 1, 2 \dots$ ). It can be seen that the harmonics with orders of  $nP_s/2$  are mainly generated by the PM-MMF, and the harmonics with orders of  $|nP_s/2 \pm kP_r|$  are produced by the field modulation effect of the salient rotor teeth. In addition, the amplitudes of the third (0.43T) and ninth (0.54T) harmonics are the largest ( $nP_s/2, n = 1, 3$ ), which further affects the contribution of the

harmonic torque. Figure 6 shows the PM flux density harmonic distributions for the front and rear module units, verifying the analytical results for the PM field modulation in AMA-FRPM machines.



**Figure 6.** PM flux density harmonic distribution for AMA-FRPM machine.

The PM-MMF of the two modules in the AMC-FRPM machine can be expressed as:

$$F_{PM}(\theta) = \pm \sum_{n=1}^{\infty} F_{PM-AMCn} \sin(nP_s\theta), \quad (6)$$

where  $F_{PM-AMCn}$  is the harmonic coefficient of the PM-MMF in the AMC-FRPM machine, which is defined as:

$$F_{PM-AMCn} = \frac{2F_{PM-AMC}}{n\pi} \left\{ \cos\left(\frac{nP_s\beta_{s-AMC}}{2}\right) - \cos\left[nP_s\left(\frac{\beta_{s-AMC}}{2} + \theta_{PM-AMC}\right)\right] \right\}, \quad (7)$$

According to Equation (6), the harmonics of the PM-MMF in the AMC-FRPM machine mainly include orders of  $nP_s$  ( $n = 1, 2, \dots$ ). Moreover, it can be seen from Equation (7) that the harmonic amplitude of the PM-MMF gradually decreases with the increase in the harmonic order. Thus, the amplitude of the sixth harmonic is the highest. The results are consistent with the FEA results shown in Figure 4. Furthermore, the trend for the variation in the PM-MMF harmonics in AMC-FRPM machines is different from that for AMA-FRPM machines, which affects the harmonic torque contributions of the two machines.

The magnetic permeance model for the salient-pole rotor of the AMC-FRPM machine is the same as that for the AMA-FRPM machine. Therefore, the PM air-gap flux densities of the front and rear module units can be expressed as:

$$B_{AMC}(\theta, t) = \pm \sum_{n=1}^{\infty} \lambda_{0-AMC} F_{PM-AMCn} \sin(nP_s\theta) \pm \sum_{n=1}^{\infty} \sum_{k=1}^{\infty} \frac{\lambda_{k-AMC} F_{PM-AMCn}}{2} \sin[(nP_s \pm kP_r)\theta \pm kP_r(\omega_r t + \theta_0)] \quad (8)$$

The prominent harmonic orders in the AMC-FRPM machine are  $|nP_s \pm kP_r|$ , ( $n = 1, 2, \dots, k = 0, 1, 2, \dots$ ). The harmonics with orders of  $nP_s$  are mainly generated by the PM-MMF, and those with orders of  $|nP_s \pm kP_r|$  are generated by the modulated field resulting from the salient-pole rotor. It can be seen from Figure 7 that the analytical results agree well with the FEA harmonic distributions. In addition, the 2nd, 6th, 12th, and 14th harmonics of the air-gap flux density in AMC-FRPM machines are the main components, and the harmonics of the 6th order have the largest amplitude ( $nP_s, n = 1$ ) at 0.65T. Therefore, the AMC-FRPM machine and AMA-FRPM machine exhibit different harmonic distributions for the PM flux density.

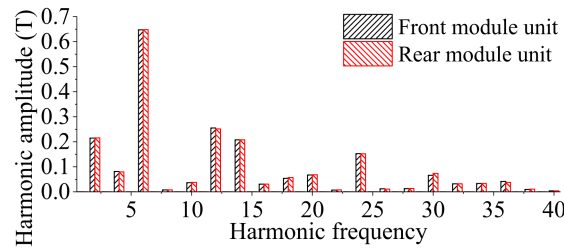


**Figure 7.** PM air-gap flux density and harmonic distribution for AMC-FRPM machine.

For the PM-MMF analysis, the geometric parameters of AM-FRPM machines with different magnetization methods are considered to be the same. Thus, the PM-MMF amplitudes  $F_{PM-AMA}$  and  $F_{PM-AMC}$  are identical. According to Equations (5) and (8), the amplitude of the ninth harmonic in the AMA-FRPM machine is 0.85 times that of the sixth harmonic in the AMC-FRPM machine, which is verified by the FEA shown in Figures 6 and 7.

### 3.2. Cogging Torque

The cogging torque  $T_{cog}$  of AM-FRPM machines can be expressed using Equation (9) [22], where  $\mu_0$  is the permeability and  $V$  is the air-gap volume:

$$T_{cog}(\alpha) = -\frac{\partial}{\partial \alpha} \left( \frac{1}{2\mu_0} \int B_g^2(\theta, \alpha) dV \right) - \frac{\partial}{\partial \alpha} \left( \frac{1}{2\mu_0} \int F_{PM}^2(\theta) \lambda^2(\theta, \alpha) dV \right) \quad (9)$$

The cogging torques of the front and rear modular units can be expressed using Equations (10) and (11), respectively, when Equation (12) is satisfied:

$$T_{cogf} = \frac{(D_{si}^2 - D_{ro}^2) \pi l_a P_r}{16\mu_0} \sum_{k=1}^{\infty} k F_{PMn} \lambda_k \sin[kP_r(\omega_r t + \theta_0)], \quad (10)$$

$$T_{cogr} = \frac{(D_{si}^2 - D_{ro}^2) \pi l_a P_r}{16\mu_0} \sum_{k=1}^{\infty} k F_{PMn} \lambda_k \sin[kP_r(\omega_r t + \theta_0) + k\pi], \quad (11)$$

$$k = \frac{j \text{LCM}(P_s, P_r)}{P_r}, \quad (12)$$

where  $\text{LCM}(P_s, P_r)$  is the lowest common multiple of  $P_s$  and  $P_r$ .  $D_{si}$  is the inner diameter of the stator,  $D_{ro}$  is the outer diameter of the rotor, and  $n = kP_r/P_s$  in the PM-MMF coefficient  $F_{PMn}$ .

According to Equations (10) and (11), the cogging torques of the front and rear module units are opposite when  $k$  is an odd number. The harmonics with odd orders in the cogging torque are then canceled. The  $P_s/P_r$  combinations for AM-FRPM machines with cogging torque harmonic suppression are listed in Table 1. For  $6s/8p$  AM-FRPM machines, the prominent harmonics of the cogging torque are the multiples of three and the odd harmonics cancel each other, as shown in Figures 8 and 9. In addition, the cogging torques of AMA-FRPM and AMC-FRPM machines are 1.2 Nm and half that of the single-module machine. Therefore, the  $6s/8p$  AM-FRPM machines with a modular structure have lower cogging torque.

**Table 1.** Combinations of AM-FRPM machines.

| $P_s$ | $P_r$             | $K$  |
|-------|-------------------|------|
| 6     | 8, 10, 14, 16     | $3j$ |
| 12    | 8, 16             | $3j$ |
|       | 10, 14            | $6j$ |
| 18    | 6                 | $3j$ |
|       | 8, 10, 12, 14, 16 | $9j$ |

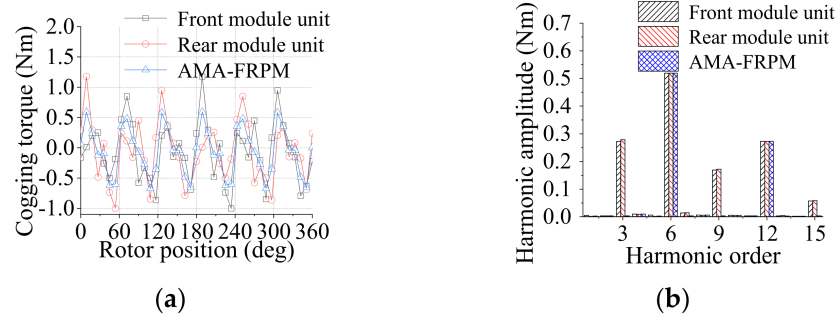


**Figure 8.** Cogging torques of the AMA-FRPM machine and a single module. (a) Cogging torque waveforms. (b) Harmonic distributions.

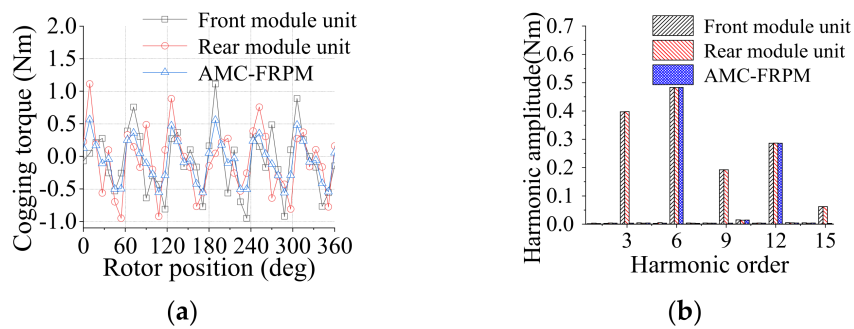


**Figure 9.** Cogging torques of the AMC-FRPM machine and a single module. (a) Cogging torque waveforms. (b) Harmonic distributions.

### 3.3. Modulation Principle for Armature Reaction Magnetic Field in AM-FRPM Machines

AM-FRPM machines utilizing AMA and AMC methods employ toroidal armature windings, as shown in Figure 1. The armature reaction MMF distributions are different from those of FRPM machines with concentrated windings. Thus, the armature reaction air-gap MMF  $F_{Wg\_gap}$  for the AMA-FRPM machine can be analyzed using the armature reaction magnetic circuit, as shown in Figure 10. Here,  $F_{W-AMA\_A1}$  and  $F_{W-AMA\_B1}$  are the armature reaction MMFs,  $\psi_a$  is the armature reaction flux linkage, and  $\Lambda_{gap}$  is the air-gap magnetic permeability. Equation (13) is the armature reaction MMF equation for the AMA-FRPM machine. The armature reaction air-gap MMF distribution can thus be obtained, as shown in Figure 11.

$$\begin{cases} F_{W-AMA-A1} = 2\Lambda_{gap}\psi_{a1} - \Lambda_{gap}\psi_{a2} + \Lambda_{gap}\psi_{a3} \\ F_{W-AMA-B1} = -\Lambda_{gap}\psi_{a1} + 2\Lambda_{gap}\psi_{a2} - \Lambda_{gap}\psi_{a3} \\ F_{W-AMA-C1} = \Lambda_{gap}\psi_{a1} - \Lambda_{gap}\psi_{a2} + 2\Lambda_{gap}\psi_{a3} \end{cases} \quad (13)$$

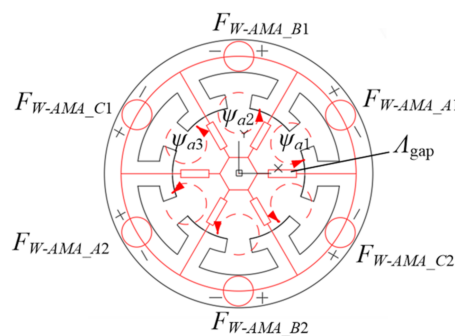


**Figure 10.** Armature reaction magnetic circuit model for AMA-FRPM machine.

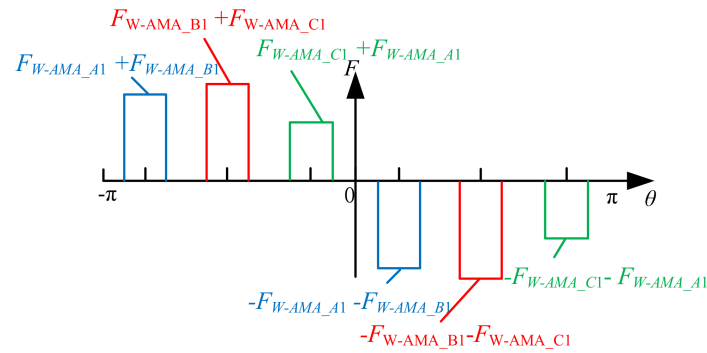


Figure 11. Armature reaction MMF model for AMA-FRPM machine.

Then, the armature reaction MMF  $F_{Wg-AMA}(\theta, t)$  for the two modular units can be obtained:

$$F_{Wg-AMA}(\theta, t) = \begin{cases} \frac{6N_{sc}I_{max}}{\pi} \sum_{i=1}^{\infty} F_{W-AMAi} \cos \varphi_1, & (i = 3r - 2, r = 1, 2, 3 \dots) \\ \frac{6N_{sc}I_{max}}{\pi} \sum_{i=1}^{\infty} F_{W-AMAi} \cos \varphi_2, & (i = 3r - 1, r = 1, 2, 3 \dots) \\ 0, & (i = 3r, r = 1, 2, 3 \dots) \end{cases} \quad (14)$$

where  $\varphi_1 = \varphi_e t + i\theta - \pi/3$  and  $\varphi_2 = \varphi_e t - i\theta - \pi/3$ .  $F_{W-AMAi}$  is the armature reaction MMF coefficient, which can be expressed as:

$$F_{W-AMAi} = \frac{\left( \sin \frac{i\pi}{2} \sin i\theta_{st} \right)}{i}, \quad (15)$$

where  $N_{sc}$  is the number of conductors per slot and  $\theta_{st}$  is half the stator-tooth width. It can be seen from Equation (14) that the harmonic orders of the armature reaction MMF can be expressed as the  $i$ th orders, where  $i$  is an odd number and does not include harmonics of multiples of three. The harmonic distribution of the armature reaction MMF for 6s/8p AMA-FRPM machines determined with FEA mainly includes the 1st, 5th, and 11th harmonics, as shown in Figure 12.

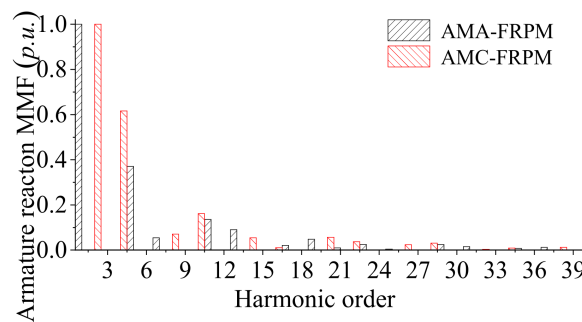


Figure 12. Armature reaction MMF harmonic distribution for AM-FRPM machines.

When  $i = 3r - 2$  ( $r = 1, 2, 3 \dots$ ), the armature reactive air-gap flux density for the AMA-FRPM machine can be obtained as:

$$B_{AMA}(\theta, t) = \frac{6N_{sc}I_{max}}{\pi} \lambda_{0-AMC} \sum_{i=1}^{\infty} F_{W-AMAi} \cos \left( \omega_e t + i\theta - \frac{\pi}{3} \right) + \frac{3N_{sc}I_{max}}{\pi} \sum_{i=1}^{\infty} \sum_{k=1}^{\infty} \lambda_{k-AMC} F_{W-AMAi} (\cos \alpha_{AMA} + \cos \beta_{AMA}) \quad (16)$$

$\alpha_{AMA}$  and  $\beta_{AMA}$  can be expressed using Equation (17), where  $d = 0$  for the front module unit and  $d=1$  for the rear module unit:

$$\begin{cases} \alpha_{AMA} = (kP_r + i)\theta + (k + 1)P_r\omega_r t + kP_r(\theta_0 + d\frac{\pi}{8}) - \frac{\pi}{3} \\ \beta_{AMA} = (kP_r - i)\theta + (k - 1)P_r\omega_r t + kP_r(\theta_0 + d\frac{\pi}{8}) + \frac{\pi}{3} \end{cases} \quad (17)$$

When  $i = 3r - 1$  ( $r = 1, 2, 3 \dots$ ), the expression for the air-gap flux density  $B_{AMA}(\theta, t)$  is:

$$\begin{aligned} B_{AMA}(\theta, t) = & \frac{6N_{sc}I_{max}}{\pi} \lambda_{0-AMC} \sum_{i=1}^{\infty} F_{W-AMAi} \cos(\omega_e t - i\theta - \frac{\pi}{3}) \\ & \frac{3N_{sc}I_{max}}{\pi} \sum_{i=1}^{\infty} \sum_{k=1}^{\infty} \lambda_{k-AMC} F_{W-AMAi} (\cos \alpha_{AMA} + \cos \beta_{AMA}), \end{aligned} \quad (18)$$

$\alpha_{AMA}$  and  $\beta_{AMA}$  can be expressed using Equation (19), where  $d = 0$  for the front module unit and  $d = 1$  for the rear module unit:

$$\begin{cases} \alpha_{AMA} = (kP_r - i)\theta + (k - 1)P_r\omega_r t + kP_r(\theta_0 + d\frac{\pi}{8}) - \frac{\pi}{3} \\ \beta_{AMA} = (kP_r + i)\theta + (k + 1)P_r\omega_r t + kP_r(\theta_0 + d\frac{\pi}{8}) + \frac{\pi}{3} \end{cases} \quad (19)$$

According to Equations (16) and (18), the main harmonic order for the armature reaction air-gap flux density is  $|kP_r \pm i|$  ( $i = 1, 5, 7 \dots, k = 0, 1, 2 \dots$ ), and all are odd harmonics. The  $i$ th harmonic is directly generated by the armature reaction MMF, while the harmonics with orders of  $|kP_r \pm i|$  are mainly generated by the salient rotor modulation. Figure 13 shows the air-gap flux density harmonic distributions for the armature magnetic fields of the front and rear module units of the AMA-FRPM machine, verifying the correctness of the armature magnetic field modulation analytical results. It can be seen from Equations (16) and (18) that the amplitudes of the third and ninth harmonics are  $3N_{sc}I_{max}\lambda_{k-AMC}F_{W-AMAi}/\pi$ . Therefore, the amplitude of the ninth harmonic of the air-gap flux density is greater than that of the third harmonic, which is consistent with the FEA results shown in Figure 13. Hence, the ninth harmonic contributes a greater harmonic component to the electromagnetic torque.

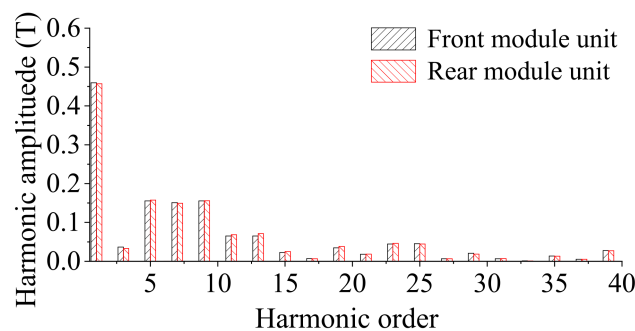


Figure 13. Armature reaction air-gap flux density harmonic distributions for AMA-FRPM machine.

For the AMC-FRPM machine, the armature reaction air-gap MMF distribution  $F_{Wg-AMC}(\theta, t)$  can be expressed using Equation (20):

$$F_{Wg-AMC}(\theta, t) = \begin{cases} \frac{2\sqrt{3}N_{sc}I_{max}}{\pi} \sum_{i=1}^{\infty} F_{W-AMCi} \cos \varphi_3, & (i = 3r - 2, r = 1, 2, 3 \dots) \\ \frac{2\sqrt{3}N_{sc}I_{max}}{\pi} \sum_{i=1}^{\infty} F_{W-AMCi} \cos \varphi_4, & (i = 3r - 1, r = 1, 2, 3 \dots) \\ 0, & (i = 3r, r = 1, 2, 3 \dots) \end{cases} \quad (20)$$

where  $\varphi_3 = \omega_e t + i\theta - \pi/3$ ,  $\varphi_4 = \omega_e t - i\theta - \pi/3$ .  $F_{W-AMCi}$  is the armature reaction MMF coefficient:

$$F_{W-AMCi} = \frac{\cos \frac{i\pi}{2} \sin i\theta_{st}}{i}, \quad (21)$$

According to Equation (20), the main harmonic order of the armature reaction MMF is the  $i$ th order, where  $i$  is an even number and does not include harmonics of multiples of three. The harmonic distribution of the armature reaction MMF is shown in Figure 12.

When  $i = 3r - 2$  ( $r = 1, 2, 3 \dots$ ),  $B_{AMC}(\theta, t)$  can be expressed as:

$$B_{AMC}(\theta, t) = \frac{2\sqrt{3}N_{sc}I_{max}}{\pi} \lambda_{0-AMC} \sum_{i=1}^{\infty} F_{W-AMC}i \cos(\omega_e t + i\theta - \frac{\pi}{3}) + \frac{\sqrt{3}N_{sc}I_{max}}{\pi} \sum_{i=1}^{\infty} \sum_{k=1}^{\infty} \lambda_{k-AMC} F_{W-AMC}i (\cos \alpha_{AMC} + \cos \beta_{AMC}) \quad (22)$$

The parameters  $\alpha_{AMC}$  and  $\beta_{AMC}$  can be expressed using Equation (23), where  $d=0$  for the front module unit and  $d = 1$  for the rear module unit:

$$\begin{cases} \alpha_{AMC} = (kP_r + i)\theta + (k + 1)P_r\omega_r t + kP_r(\theta_0 + d\frac{\pi}{8}) - \frac{\pi}{3} \\ \beta_{AMC} = (kP_r - i)\theta + (k - 1)P_r\omega_r t + kP_r(\theta_0 + d\frac{\pi}{8}) + \frac{\pi}{3} \end{cases} \quad (23)$$

When  $i = 3r - 1$  ( $r = 1, 2, 3 \dots$ ),  $B_{AMC}(\theta, t)$  can be expressed as:

$$B_{AMC}(\theta, t) = \frac{2\sqrt{3}N_{sc}I_{max}}{\pi} \lambda_{0-AMC} \sum_{i=1}^{\infty} F_{W-AMC}i \cos(\omega_e t - i\theta - \frac{\pi}{3}) + \frac{\sqrt{3}N_{sc}I_{max}}{\pi} \sum_{i=1}^{\infty} \sum_{k=1}^{\infty} \lambda_{k-AMC} F_{W-AMC}i (\cos \alpha_{AMC} + \cos \beta_{AMC}) \quad (24)$$

$\alpha_{AMC}$  and  $\beta_{AMC}$  can be obtained using Equation (25), where  $d=0$  for the front module unit and  $d = 1$  for the rear module unit.

$$\begin{cases} \alpha_{AMC} = (kP_r - i)\theta + (k - 1)P_r\omega_r t + kP_r(\theta_0 + d\frac{\pi}{8}) - \frac{\pi}{3} \\ \beta_{AMC} = (kP_r + i)\theta + (k + 1)P_r\omega_r t + kP_r(\theta_0 + d\frac{\pi}{8}) + \frac{\pi}{3} \end{cases} \quad (25)$$

According to Equations (22) and (24), the main harmonic numbers for the armature reaction air-gap flux density are  $|kP_r \pm i|$ , ( $i = 2, 4, 8 \dots, k = 0, 1, 2 \dots$ ), which are even. The  $i$ th harmonic (excluding multiples of three) is directly generated by the armature reaction MMF, while the rotor salient-pole modulation mainly generates the  $|kP_r \pm i|$  harmonic. Figure 14 shows the air-gap flux density harmonic distributions for the armature magnetic fields of the front and rear module units of the AMC-FRPM machine. The correctness of the armature reaction magnetic field modulation analytical results is verified.

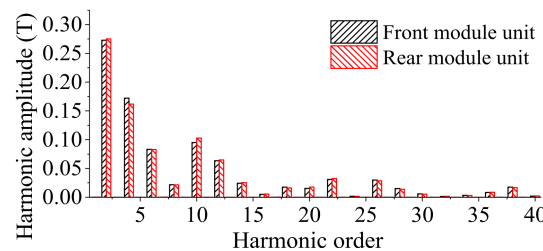


Figure 14. Armature reaction air-gap flux density harmonic distributions for AMC-FRPM machine.

According to Equations (16) and (22), the harmonic amplitudes of the armature reaction air-gap flux densities of AMA-FRPM and AMC-FRPM machines are  $3N_{sc}I_{max}F_{W-AMA}i/\pi$  and  $\sqrt{3}N_{sc}I_{max}F_{W-AMC}i/\pi$ , respectively. According to Equations (14) and (20), the MMF fundamental harmonic amplitude for the AMA-FRPM machine  $F_{W-AMA1}$  is 1.85 times that of the second harmonic for the AMC-FRPM machine  $F_{W-AMC2}$ . Then, the amplitude of the ninth harmonic ( $|kP_r + i|, i = 1, k = 1$ ) of the air-gap flux density of the AMA-FRPM machine is 1.85 times that of the sixth harmonic ( $|kP_r - i|, i = 2, k = 1$ ) of the AMC-FRPM machine, which is consistent with the FEA results. Therefore, based on the analytical results for the PM and armature reaction magnetic fields, the torque contribution of the sixth

harmonic of the air-gap flux density from the AMC-FRPM machine is smaller than that of the ninth harmonic from the AMA-FRPM machine.

### 3.4. Electromagnetic Torque

The torque production mechanism in AM-FRPM machines using the AMA and AMC methods can be determined based on magnetic loading  $B_{gv}$  and electric loading  $K_{sv}$  [23]. The harmonic contributions to the torque of the two AM-FRPM machines are shown in Figure 15. It can be seen that the ninth harmonic in the AMA-FRPM machine generates 82% of the total torque. The sixth harmonic in the AMC-FRPM machine is the main harmonic contributing to the torque, accounting for 63% of the total torque. Therefore, the torque output capability of AM-FRPM machines can be analyzed according to the torque component generated by the fundamental harmonic from the air-gap magnetic field. It is worth noting that the output torque generated by the sixth ( $nP_s$ , ( $n = 1$ )) harmonic in the AMC-FRPM machine is 6.8 Nm, which is only 52% of the torque component of the ninth ( $nP_s/2$ , ( $n = 3$ )) harmonic of the AMA-FRPM machine. Therefore, the AMA-FRPM machine can effectively use the ninth ( $nP_s/2$ , ( $n = 3$ )) harmonic with a higher amplitude in the PM magnetic field and armature reaction magnetic field to generate higher output torque.

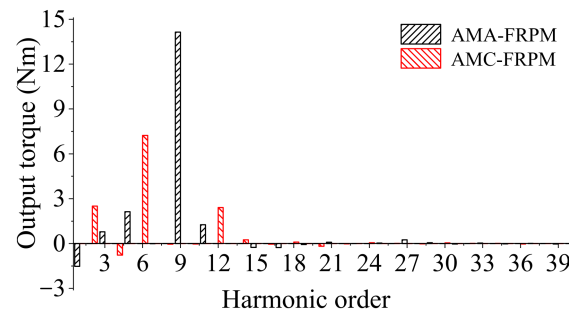


Figure 15. Contributions of the air-gap harmonics to the torque in the two AM-FRPM machines.

## 4. Electromagnetic Characteristics Analysis

In this section, the electromagnetic characteristics of two types of AM-FRPM machines and a traditional FRPM machine are compared. To objectively and fairly analyze the advantages and disadvantages of the proposed AM-FRPM machines, the stator outer diameter, axial length, air-gap length, and other parameters of the three machines, as well as the materials used in each part, were kept consistent, as shown in Table 2. The rated current density, rated speed, and DC bus voltage of the three machines were  $J_{sa} = 5\text{ A/mm}^2$ ,  $n = 1500\text{ r/min}$ , and  $U_{dc} = 400\text{ V}$ , respectively.

Table 2. The parameters of three FRPM machines.

| Parameters                                | AMA-FRPM | AMC-FRPM | FRPM |
|---|----------|----------|------|
| $P_s/P_r$                                 |          | $6s/8p$  |      |
| Speed $n$ (r/min)                         |          | 1500     |      |
| Stator outer diameter $D_{so}$ (mm)       |          | 128      |      |
| Stator inner diameter $D_{si}$ (mm)       |          | 70.4     |      |
| Effective shaft length $l_a$ (mm)         |          | 75       |      |
| Rotor inner diameter $D_{ri}$ (mm)        |          | 22       |      |
| Air-gap length $g$ (mm)                   |          | 0.35     |      |
| Rotor pole arc $\theta_{rt}$ (deg)        |          | 20       |      |
| Stator tooth width $\theta_{st}$ (deg)    | 41.5     |          | 40.0 |
| PM thickness $l_{pm}$ (mm)                | 1.60     |          | 1.84 |
| PM width $\theta_{pm}$ (deg)              | 18.5     |          | 20.0 |
| PM notch width $\theta_{pmg_{gap}}$ (deg) | 4.5      |          | 0    |
| PM magnetization mode                     | NSSN     | NSNS     | NSNS |
| Silicon steel sheet material              |          | 50WW470  |      |
| PM material                               |          | N35SH    |      |
| Number of turns of winding                | 64       | 117      | 107  |
| Wire diameter (mm)                        | 2.01     | 1.53     | 1.01 |

The FRPM machine's back-EMF amplitude was 203.5V, as shown in Figure 16, which was 15.3% and 45.0% higher than those of the AMC-FRPM and AMA-FRPM machines, respectively. In addition, the harmonic content of the back-EMF of the AMC-FRPM machine was 2.1%, which was 0.3% and 3.4% lower than those of the AMA-FRPM and FRPM machines.

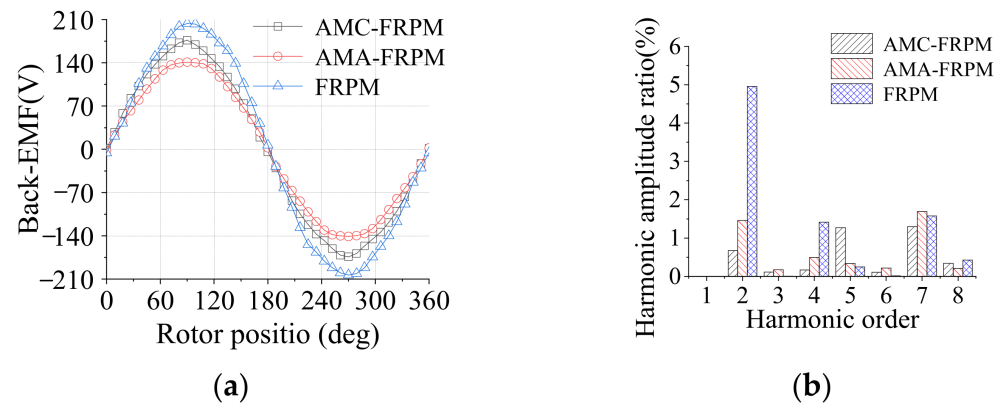


Figure 16. Back-EMFs of the three machines. (a) Back-EMF waveforms. (b) Harmonic distributions.

Figure 17a compares the cogging torques of the three machines. The cogging torques of the AMA-FRPM and AMC-FRPM machines were approximately equal to 1.0 Nm, 38.5% that of the FRPM machine. The reason was that the axial modular cooperation structure effectively suppressed the cogging torque. Figure 17b shows the output torques of the three machines with rated current density. The output torque of the AMA-FRPM machine was 13.83 Nm, 1.3 times and 2.0 times those of the AMC-FRPM and FRPM machines. The torque ripple of the AMA-FRPM machine was 8%, which was 3% and 26.6% lower than those of the AMC-FRPM machine and FRPM machine. Figure 18 shows the overload capacities of the three machines. It can be seen that the overload capacities of the FRPM machine and AMC-FRPM machine were better than that of the AMA-FRPM machine. It can be seen from Figure 19 that this was because the magnetic field of the stator teeth and yoke in the AMA-FRPM machine was seriously saturated. However, the output torque of the AMA-FRPM machine was the highest among the three machines at  $J_{sa} < 7.5 \text{ A/mm}^2$ . In addition, the efficiency of the AMC-FRPM machine was 89.3%, which was 0.4% and 1.9% higher than the efficiencies of the AMA-FRPM machine and FRPM machine.

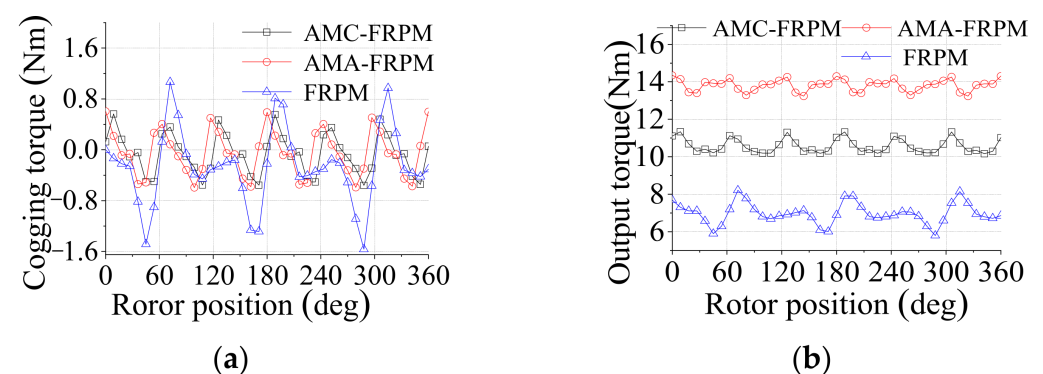


Figure 17. Torque performances of the three machines. (a) Cogging torque. (b) Output torque.

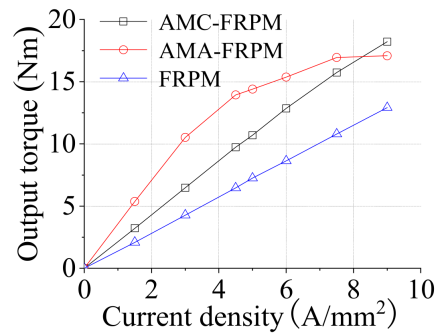


Figure 18. Output torques with different current densities for the three machines.

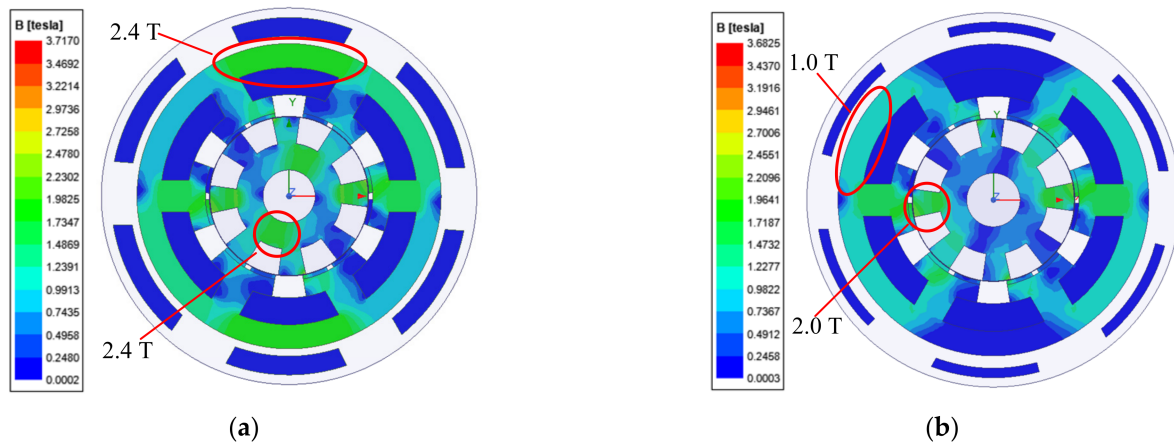


Figure 19. Flux density distributions for AM-FRPM machines. (a) AMA-FRPM. (b) AMC-FRPM.

The electromagnetic properties of the AMA-FRPM machine, AMC-FRPM machine, and FRPM machine are shown in Table 3.

Table 3. Comparison of electromagnetic characteristics of AM-FRPM and FRPM machines.

| Parameters                               | AMA-FRPM | AMC-FRPM | FRPM   |
|--|----------|----------|--------|
| Cogging torque $T_{cog}$ (Nm)            | 1.20     | 1.12     | 2.6    |
| Torque $T_e$ (Nm)                        | 13.83    | 10.60    | 7.00   |
| Torque ripple $T_{rip}$ (%)              | 8.00     | 11.00    | 34.60  |
| PM utilization ratio $K_T/V_{PM}$ (Nm/L) | 874.2    | 670.0    | 340.0  |
| Torque density $K_T/V$ (Nm/L)            | 14.33    | 10.98    | 7.22   |
| Power $P_{out}$ (W)                      | 2420.4   | 1671.2   | 1095.0 |
| PM eddy current loss $P_{PM}$ (W)        | 29.72    | 28.00    | 43.00  |
| Core loss $P_{Fe}$ (W)                   | 76.77    | 38.50    | 20.00  |
| Copper loss $P_{Cu}$ (W)                 | 147.02   | 133.0    | 94.00  |
| Efficient $\eta$ (%)                     | 89.83    | 89.30    | 87.40  |

To evaluate the performance and disadvantages of the proposed machine in electric vehicle and hybrid electric vehicle applications, a comprehensive comparison of the AMA-FRPM machine and the Toyota Prius 2010 IPM machine was conducted. To ensure a fair comparison, the stator outer diameter ( $D_{s0} = 264$  mm), axial length ( $l_a = 50.16$  mm), air-gap ( $g = 0.73$  mm), rated speed ( $n = 2770$  r/min), current density ( $J_{sa} = 10.2$  A/mm<sup>2</sup>), and other parameters of the two machines were kept consistent.

Figure 20a shows a comparison of the cogging torques of the two machines. The cogging torque of the AMA-FRPM machine was 0.34 Nm, 11.5% that of the Prius IPM machine. Figure 20b shows the output torques of the two machines at 10.2 A/mm<sup>2</sup>. It can be seen that the output torque of the AMA-FRPM machine was 116.07Nm, which was

24.78% greater than that of the Prius IPM machine. In addition, the torque ripple of the AMA-FRPM machine was 3.1%, which was 8.79% lower than that of the Prius IPM machine. Therefore, the AMA-FRPM machine had a better torque output capacity and lower torque ripple, making it suitable for electric vehicle drive systems.

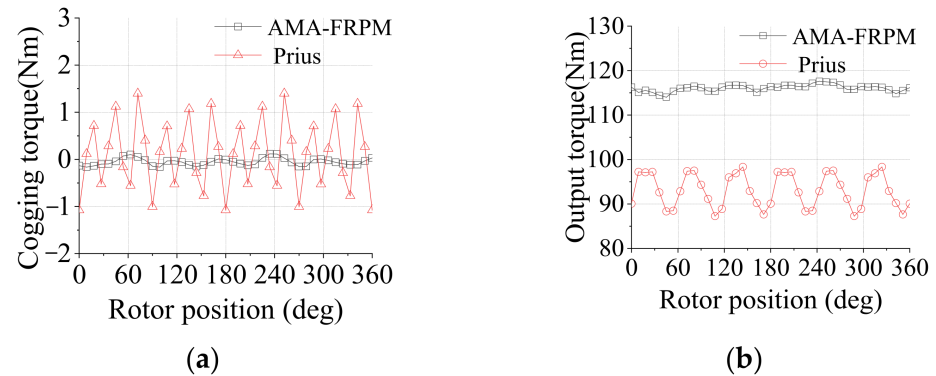


**Figure 20.** Torque performances of AMA-FRPM and Prius machines. (a) Cogging torque. (b) Output torque.

### 5. Experiment Validation

To verify the previous analysis, FRPM machine and AM-FRPM machine prototypes were manufactured and tested, as shown in Figure 21. The specific structural parameters are shown in Table 2.

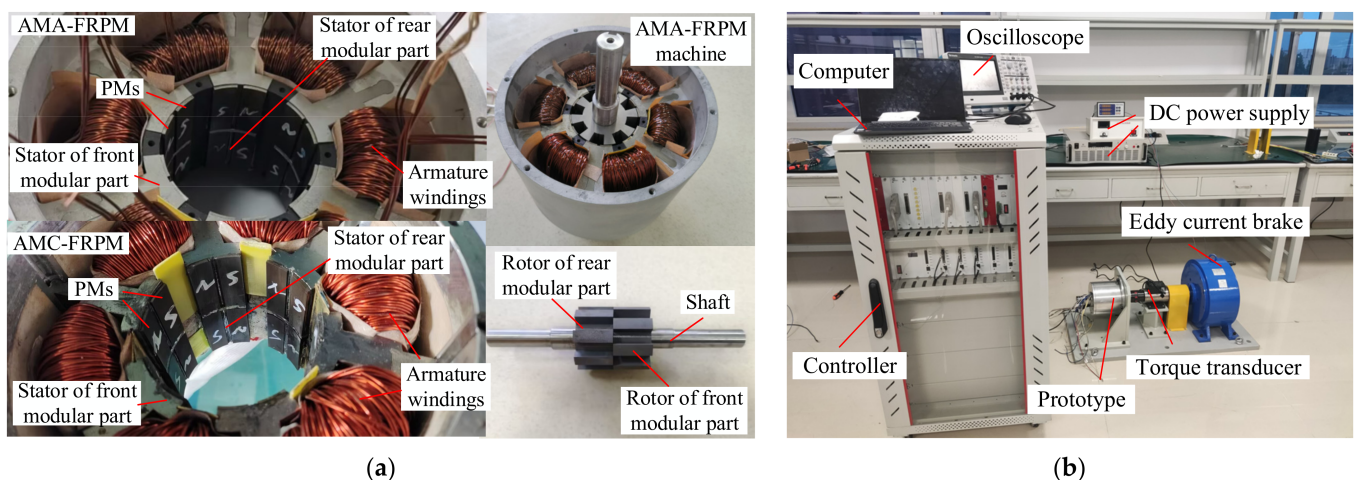


**Figure 21.** Prototypes and experiment platform. (a) Prototype machines. (b) Experiment platform.

The tested back-EMFs of the AM-FRPM and FRPM machines are shown in Figure 22. The experimental waveforms of the three prototypes almost coincided with the simulation waveforms. The back-EMF amplitude of the AMC-FRPM machine was 174 V, which was 5 V lower than the simulated analysis. Moreover, it can be seen from the harmonic analysis that the harmonic content of the tested back-EMF was 3.3%, which was 1.1% larger than the FEA result. In addition, the measured back-EMF amplitude of the AMA-FRPM machine was 128 V, 12 V lower than the simulated analysis. In addition, its harmonic content was 2.3%, which was 0.1% lower than the FEA result. The simulated and experimental values for the back-EMF fundamental wave amplitudes of the two FRPM machines were both 200 V. The harmonic content of the measured back-EMF was 3.1%, which was 1% greater than the FEA result.

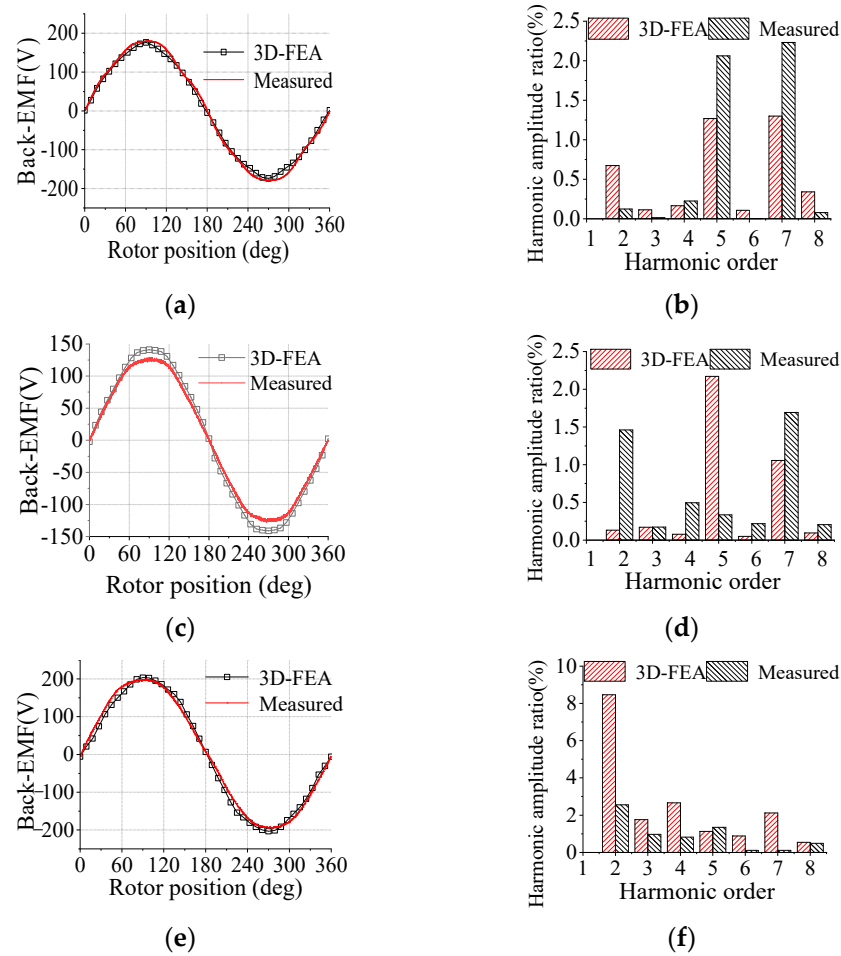


**Figure 22.** Back-EMF waveforms for the two types of machines. (a,b) AMC-FRPM machine. (c,d) AMA-FRPM machine. (e,f) FRPM machine.

The output torques for the two machines with different current densities are shown in Figure 23. It can be seen that the simulated and the measured values had good consistency. At the rated current density of 5 A/mm<sup>2</sup>, the measured output torque of the AMC-FRPM machine was 9.5 Nm, which was 0.66 Nm lower than the 3D FEA result. Moreover, the output torque of the FRPM machine measured at the same current density was 6.6 Nm, which was 0.1 Nm lower than the 3D FEA result. Through the experimental analysis, the correctness of the previous research was verified.

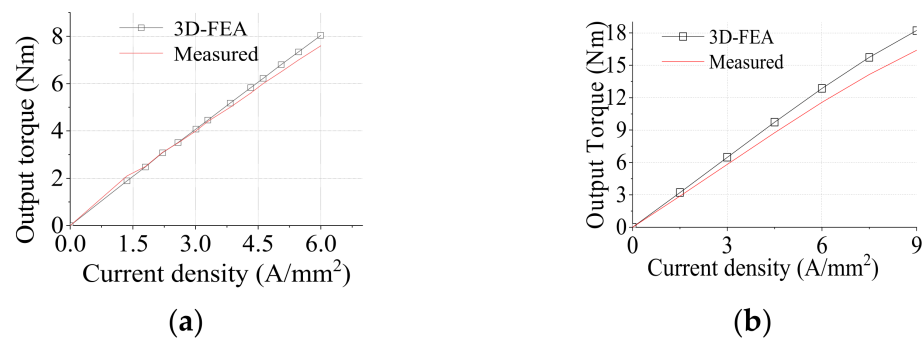


**Figure 23.** Output torque for two machines with different current densities. (a) AMC-FRPM. (b) FRPM.

## 6. Conclusions

In this paper, a novel type of AM-FRPM machine was proposed. Based on air-gap magnetic field modulation theory, the optimal harmonic coordination method was proposed, and the principle for the suppression of the cogging torque in the AM-FRPM machine was expounded. The experiment verified that the AM-FRPM machine has the advantages of high output torque and low torque ripple, which makes it an attractive candidate for electric vehicle (EV) and hybrid electric vehicle (HEV) applications. The conclusions are summarized as follows.

- (1) The electromagnetic torque of the AMC-FRPM machine is mainly generated by the fundamental harmonic of the PM-MMF ( $nP_s$ , ( $n = 1$ )), while the torque of the AMA-FRPM machine is mainly generated by the third harmonic of the PM-MMF ( $nP_s/2$  ( $n = 3$ ));
- (2) With regard to the armature reaction air-gap flux density, the amplitude of the ninth ( $nP_s/2$  ( $n = 3$ )) harmonic in the AMA-FRPM machine is 1.85 times that of the sixth ( $nP_s$ , ( $n = 1$ )) harmonic in the AMC-FRPM machine. Moreover, the corresponding difference in the harmonic amplitudes between the PM magnetic fields of the two machines is only 15%. The ninth harmonic of the AMA-FRPM machine generates higher output torque, 1.92 times that of the sixth harmonic of the AMC-FRPM machine, with a better harmonic utilization rate;
- (3) Due to the toroidal winding and axial module structure, the AM-FRPM machines have the advantages of higher output torque and lower torque ripple compared to FRPM machines. The AMA-FRPM machine has the highest torque output capacity, and the AMC-FRPM machine has a stronger overload capacity;
- (4) By analyzing the cogging torque suppression mechanism, it was found that the AM-FRPM machines can cancel the odd-harmonic component of the cogging torque through the combination of module units, providing guidance for the selection of stator-slot and rotor-pole combinations;
- (5) Compared to the Prius IPM machine, the AMA-FRPM machine has a better torque output capacity at  $J_{sa} < 13 \text{ A/mm}^2$ . Therefore, the AM-FRPM machine holds promise for application in EVs and HEVs.

**Author Contributions:** Conceptualization, W.H.; methodology, P.S.; software, Y.S.; writing—original draft preparation, L.C. and P.S.; writing—review and editing, P.S. and Y.L.; supervision, S.L. and W.H.; All authors have read and agreed to the published version of the manuscript.

**Funding:** National Natural Science Foundation of China: 52007048, 52130710; Natural Science Foundation of Hebei Province: E2021202144; State Key Laboratory of Reliability and Intelligence of Electrical Equipment Fund: EERI\_OY2020010.

**Data Availability Statement:** The data discussed in this research paper are provided on request from the corresponding author. The data are confidential.

**Conflicts of Interest:** The authors declare no conflict of interest.

## References

1. Fan, W.; Zhu, X.; Quan, L.; Wu, W.; Xu, L.; Liu, Y. Flux-Weakening Capability Enhancement Design and Optimization of a Controllable Leakage Flux Multilayer Barrier PM Motor. *IEEE Trans. Ind. Electron.* **2020**, *68*, 7814–7825. [\[CrossRef\]](#)
2. Jiang, M.; Zhu, X.; Xiang, Z.; Quan, L.; Que, H.; Yu, B. Suppression of Torque Ripple of a Flux-Switching Permanent Magnet Motor in Perspective of Flux-Modulation Principle. *IEEE Trans. Transp. Electr.* **2021**, *8*, 1116–1127. [\[CrossRef\]](#)
3. Yang, K.; Zhao, F.; Wang, Y.; Bao, Z. Consequent-Pole Flux Reversal Permanent Magnet Machine With Halbach Array Magnets in Rotor Slot. *IEEE Trans. Magn.* **2020**, *57*, 1–5. [\[CrossRef\]](#)
4. Li, H.; Zhu, Z.Q.; Hua, H. Comparative Analysis of Flux Reversal Permanent Magnet Machines With Toroidal and Concentrated Windings. *IEEE Trans. Ind. Electron.* **2019**, *67*, 5278–5290. [\[CrossRef\]](#)
5. Li, H.; Zhu, Z.Q. Influence of Adjacent Teeth Magnet Polarities on the Performance of Flux Reversal Permanent Magnet Machine. *IEEE Trans. Ind. Appl.* **2018**, *55*, 354–365. [\[CrossRef\]](#)
6. Meng, Y.; Fang, S.; Pan, Z.; Liu, W.; Qin, L. Design and Analysis of a New Partitioned Stator Hybrid-Excited Flux Reversal Machine With Dual-PM. *IEEE Trans. Magn.* **2021**, *58*, 1–6. [\[CrossRef\]](#)

7. Xie, K.; Li, D.; Qu, R.; Yu, Z.; Gao, Y.; Pan, Y. Analysis of a Flux Reversal Machine With Quasi-Halbach Magnets in Stator Slot Opening. *IEEE Trans. Ind. Appl.* **2018**, *55*, 1250–1260. [[CrossRef](#)]
8. Yang, H.; Lin, H.; Zhu, Z.Q.; Lyu, S.; Liu, Y. Design and Analysis of Novel Asymmetric-Stator-Pole Flux Reversal PM Machine. *IEEE Trans. Ind. Electron.* **2019**, *67*, 101–114. [[CrossRef](#)]
9. Vidhya, B.; Srinivas, K.N. Effect of stator permanent magnet thickness and rotor geometry modifications on the minimization of cogging torque of a flux reversal machine. *Turk. J. Electr. Eng. Comput. Sci.* **2017**, *25*, 4907–4922. [[CrossRef](#)]
10. Yuansheng, Z.; Baoquan, K.; Xiaokun, Z. A Study of Torque Characteristics of a Novel Flux Reversal Machine. In *2019 22nd International Conference on Electrical Machines and Systems (ICEMS)*; IEEE: New York, NY, USA, 2019; pp. 1–5.
11. Kim, T.H.; Won, S.H.; Bong, K.; Lee, J. Reduction of cogging torque in flux-reversal machine by rotor teeth pairing. *IEEE Trans. Magn.* **2005**, *41*, 3964–3966.
12. Kim, J.H.; Li, Y.; Cetin, E.; Sarlioglu, B. Influence of Rotor Tooth Shaping on Cogging Torque of Axial Flux-Switching Permanent Magnet Machine. *IEEE Trans. Ind. Appl.* **2019**, *55*, 1290–1298. [[CrossRef](#)]
13. Ren, W.; Xu, Q.; Li, Q.; Zhou, L. Reduction of Cogging Torque and Torque Ripple in Interior PM Machines With Asymmetrical V-Type Rotor Design. *IEEE Trans. Magn.* **2016**, *52*, 1–5. [[CrossRef](#)]
14. Pan, Z.; Fang, S.; Lin, H.; Yang, H.; Qin, L.; Lyu, S. A New Hybrid-Excited Flux Reversal Arc Permanent Magnet Machine Having Partitioned Stators for Large Telescope Application. *IEEE Trans. Magn.* **2019**, *55*, 1–10. [[CrossRef](#)]
15. Zheng, Y.; Wu, L.; Zhu, J.; Fang, Y.; Qiu, L. Analysis of Dual-Armature Flux Reversal Permanent Magnet Machines With Halbach Array Magnets. *IEEE Trans. Energy Convers.* **2021**, *36*, 3044–3052. [[CrossRef](#)]
16. Qu, H.; Zhu, Z.Q. Analysis of Spoke Array Permanent Magnet Flux Reversal Machines. *IEEE Trans. Energy Convers.* **2020**, *35*, 1688–1696. [[CrossRef](#)]
17. Zhu, X.; Hua, W.; Wang, W.; Huang, W. Analysis of Back-EMF in Flux-Reversal Permanent Magnet Machines by Air Gap Field Modulation Theory. *IEEE Trans. Ind. Electron.* **2018**, *66*, 3344–3355. [[CrossRef](#)]
18. Cheng, M.; Han, P.; Hua, W. General Airgap Field Modulation Theory for Electrical Machines. *IEEE Trans. Ind. Electron.* **2017**, *64*, 6063–6074. [[CrossRef](#)]
19. Wang, P.; Hua, W.; Zhang, G.; Wang, B.; Cheng, M. Principle of Flux-Switching Permanent Magnet Machine by Magnetic Field Modulation Theory Part I: Back-Electromotive-Force Generation. *IEEE Trans. Ind. Electron.* **2021**, *69*, 2370–2379. [[CrossRef](#)]
20. Wang, P.; Hua, W.; Zhang, G.; Wang, B.; Cheng, M. Principle of Flux-Switching PM Machine by Magnetic Field Modulation Theory Part II: Electromagnetic Torque Generation. *IEEE Trans. Ind. Electron.* **2021**, *69*, 2437–2446. [[CrossRef](#)]
21. Gao, J.; Xiang, Z.; Dai, L.; Huang, S.; Ni, D.; Yao, C. Cogging Torque Dynamic Reduction Based on Harmonic Torque Counteract. *IEEE Trans. Magn.* **2022**, *58*, 1–5. [[CrossRef](#)]
22. Zhu, X.; Hua, W.; Wu, Z. Cogging torque suppression in flux-reversal permanent magnet machines. *IET Electr. Power Appl.* **2017**, *12*, 135–143. [[CrossRef](#)]
23. Su, P.; Hua, W.; Hu, M.; Wu, Z.; Si, J.; Chen, Z.; Cheng, M. Analysis of Stator Slots and Rotor Pole Pairs Combinations of Rotor-Permanent Magnet Flux-Switching Machines. *IEEE Trans. Ind. Electron.* **2019**, *67*, 906–918. [[CrossRef](#)]

**Disclaimer/Publisher’s Note:** The statements, opinions and data contained in all publications are solely those of the individual author(s) and contributor(s) and not of MDPI and/or the editor(s). MDPI and/or the editor(s) disclaim responsibility for any injury to people or property resulting from any ideas, methods, instructions or products referred to in the content.